Water adsorbed in a commercial carbon: role of nanostructure and surface chemistry

Krisztina László[1*], Orsolya Czakkel[2], Attila Domján,[3] György Sáfrán[4], Zoltán Sebestyén[3], Anna Bulátkó[1], Silvia Villar-Rodil[5], Juan M.D. Tascón[5], Erik Geissler[6]

[1] Department of Physical Chemistry and Materials Science, Faculty of Chemical Technology and Biotechnology, Budapest University of Technology and Economics, Műegyetem rkp. 3., H-1111 Budapest, Hungary laszlo.krisztina@vbk.bme.hu; bulatko.anna@edu.bme.hu

[2] Institut Laue Langevin, CS 20156, F – 38042 Grenoble Cedex 9, France czakkel@ill.eu

[3] Institute of Materials and Environmental Chemistry, HUN-REN Research Centre for Natural Sciences, Magyar tudósok körútja 2., Budapest, H-1117, Hungary; domjan.attila@ttk.hu

[4] Research Institute for Technical Physics and Materials Science, Konkoly Thege M. út 29-33, Budapest H-1121, Hungary safran.gyorgy@ek-cer.hu

[5]Instituto de Ciencia y Tecnología del Carbono, INCAR-CSIC, Francisco. Pintado Fe 26, 33011 Oviedo, Spain silvia@incar.csic.es; tascon@incar.csic.es

[6] Laboratoire Interdisciplinaire de Physique (LIPhy), Université Grenoble Alpes and CNRS, F-38000, Grenoble, France e.geissler@orange.fr
* Corresponding author

Abstract

This article investigates the spatial disposition and mobility of water molecules adsorbed at room temperature in a commercial activated amorphous carbon. Previous wide-angle X-ray scattering measurements are re-examined, together with new observations, in particular by high-resolution transmission electron microscopy, high field solid-state nuclear magnetic resonance, and pulsed field gradient nuclear magnetic resonance. The dry samples are composed largely of deformed turbostratic oxidised graphitic sheets, yielding an array of slit-pores with an average spacing of more than 0.4 nm. All the adsorbed water remains close to the aromatic substrate, and the landscape of adsorption sites is extremely heterogeneous. The water molecules are mobile. Water is initially adsorbed in small confined sites. With increasing relative humidity these develop into clusters that are spatially correlated, which spread and merge, on both sides of the graphitic sheets.

Keywords

water vapour adsorption, nanostructured carbon, SAXS, HRTEM, WAXS, solid state NMR, pulsed field gradient NMR

1 Introduction

The unique combination of their porous texture and chemical characteristics is the source of the outstanding sorption performance of nanostructured carbon materials. Porous carbons are of inherently hydrophobic nature. They are “general adsorbents”, as their interaction with most organic molecules is dominated by nonspecific, e.g., dispersion, forces. The performance on a microscopic level, however, is strongly influenced by the chemical nature of the carbon surface. The fundamentally hydrophobic surface is often decorated with non-metallic heteroatoms, most frequently and intrinsically with oxygen, acting as tuneable local polar sites [1, 2, 3, 4]. The functional groups along the surface and/or within the porous system may promote or challenge the actual performance of the porous carbon in industrial applications, including gas storage, removal of nonpolar vapours, (electro)catalysis, etc. [5, 6, 7, 8, 9].

The adsorption of water vapour on the surface of activated carbon has long been a subject of preoccupation in defining the effective surface area of high surface area carbons and in determining the effects of surface treatment on the adsorption capacity.[1, 2, 3] While macroscopic techniques like contact angle or adsorption isotherms provide an overall picture of the carbon, the nature of heteroatoms, the chemistry of the adsorption sites, as well as the distribution of the adsorbed molecules and their mobility, remain unclear. Experimental studies combined with modelling [10, 11] are an efficient means to understand the mechanism of water vapour adsorption: revealing the rate of occupation of pores of various sizes and availabilities, what are the factors affecting the uptake phenomena (e.g., pore structure and size distribution, type and density of the functional groups, their acid/base properties, etc.) [12, 13]. Monte Carlo simulations have brought to light the effect of the various O-functionalities, as well as the role of their surface distribution and relative position [7, 14].

Graphene and its derivatives allow a new approach to this area as well [15]. The particular and important role of surface oxygen groups in the water permeability of a He-impermeable graphene oxide membrane was recently demonstrated by Nair et al [16]. They propose that the GO sheets form 2D capillaries with hydrophilic and hydrophobic regions, such that their interlayer distance can be reversibly tuned through relative humidity (RH). Their opening and closing can thus be altered by a change in RH. At high RH the water vapour acts as a spacer in the oxidized regions, leaving narrow, empty percolation spaces between the hydrophobic regions of the sheets. Water molecules easily permeate through these hydrophobic capillaries, while the diffusion of other molecules is blocked by their narrowing at low RH and/or by being blocked with water at high RH.

A consensus has now developed that the functional groups act as nucleation centres for water vapour and that their surface concentration is responsible for water vapour uptake at low relative humidity [10]. The micro- and narrow mesopores fill through a cluster-mediated mechanism that differs from the Kelvin equation [17].

Several authors have performed detailed studies using X-ray and neutron scattering to determine the structure of the water adsorbed in activated carbons [12, 18, 19, 20, 21]. A later investigation, however, found that the delay time required to achieve full equilibrium with the water vapour can last as long as several weeks [22], which implies that earlier observations did not necessarily measure the adsorbed water molecules at their equilibrium positions in the sample. The principal finding of ref [22] was the large discrepancy between the water adsorption isotherms measured at short time scales by conventional techniques and those found by X-ray scattering and gravimetric methods over an extended period of several months. In this article we approach these questions in the case of water vapour adsorbed on the same commercial high surface area carbon, Norit R1 Extra, both in its raw state and in oxidised form. While some of the X-ray scattering findings were already outlined in reference [22], the aim of the present article is to reinterpret those findings in the light of new evidence. As some of the measurements reported here were conducted at different times on the same samples over several years, it is reasonable to question whether the surface chemistry of the samples remained identical throughout. The most sensitive data, those of X-ray scattering, are the same as those reported in [22], but more extensively evaluated: the only differences introduced here are a) a small correction to the wavenumbers q (amplitude of the transfer wave vector $\mathbf{q}$) in the wide angle (WAXS) region and a more detailed investigation of the X-ray intensity scattered by the adsorbed water, and b) a novel examination of the intensity ratio between the wet and dry samples in the smallest wave number region (SAXS). As to the water adsorption properties of the samples, these have remained identical, within experimental error, over the whole period.

Norit R1 Extra is a commercial activated plant based, non-graphitic carbon with high internal porosity. According to its suppliers [23] it contains small amounts of unspecified microcrystalline material. This paper, with a mind to the theoretical and modelling community, aims to present a wide range of experimental observations employing traditional gas adsorption techniques and chemical analysis methods, as well as transmission electron microscopy, wide angle X-ray scattering, high field solid-state NMR with magic angle spinning, small angle X-ray scattering, and pulsed field gradient NMR at 20 MHz, in order to investigate the state of water adsorbed on two forms of the Norit carbon: 1) the as-supplied sample, and 2) the same sample after exposure to concentrated nitric acid for 3 hours. [22] An aspect of particular interest is the study of how water molecules are adsorbed on both sides of exposed graphene sheets in the carbon.

2 Experimental

2.1 Sample preparation

A commercial high surface area granular carbon (Norit R1 Extra, Cabot Corporation) designated R1 was used as supplied. The amount of all oxygen containing functionalities except for O* increased with the oxidation, with a slight predominance of oxygen singly bonded to carbon, i.e., carbonyl and phenolic groups. Norit OX, 20 g of the as-received lignocellulose based R1 Extra was treated with 200 mL concentrated nitric acid at room temperature for 3 hours. After the oxidation this sample was thoroughly washed with distilled water and then dried.

Carbon samples for SAXS/WAXS were prepared by filling the powdered, dry carbon in thin-walled Lindemann glass capillary tubes of diameter 1.5 mm. The open capillaries were exposed to different degrees of relative humidity (RH) in closed containers for 8 weeks at 20 ºC. At the end of the preparation, the capillary tubes were flame-sealed.

2.2 Nitrogen and CO_2 adsorption

Low temperature (-196 °C) nitrogen adsorption/desorption isotherms were measured on the granular samples with an Autosorb-1 (Quantachrome, USA) apparatus. The apparent surface area was derived according to the BET model [24]. For the characterisation of the porous texture, the Dubinin-Radushkevich (DR) and Quenched Solid Density Function Theory (QSDFT) methods were employed [25, 26]. The pore size distribution (PSD) was calculated from the adsorption branch with slit/cylindrical pore geometry. Carbon dioxide isotherms were measured at 0 °C with the same volumetric instrument. Evaluation of the primary adsorption data was performed with the Quantachrome ASiQwin software (version 3.0).

2.3 Bulk and surface composition

Thermogravimetry/mass spectrometry (TG/MS) measurements were carried out in a modified Perkin-Elmer TGS-2 thermobalance coupled to a HiQuad quadrupole mass spectrometer. Approx. 9 mg of Norit R1 and Norit OX samples were heated at a rate of 20 °C min^{-1} from room temperature to 900 °C in argon atmosphere at a flow rate of 140 mL min^{-1}. A small proportion of gas and vapour evolved from the samples was introduced into the mass spectrometer through a glass-lined metal capillary transfer line heated to 300 °C. The ion source of the mass spectrometer was operated at 70 eV electron energy. The ion intensities were normalized with respect to the sample mass and to the intensity of the ^{38}Ar isotope of the carrier gas. CO and CO_2 were measured at M/Z 28 and 44, respectively.

The elemental analyses of C, H, N and O were performed in a LECO Truspec Micro CHNS microanalysis apparatus (ASTM D5373) with a LECO Truspec Micro O accessory for O analysis, while S was analyzed in a LECO S632 analysis apparatus (ASTM D4239). S and O were analyzed in different portions of sample than C, H and N. Oxygen was determined from the amounts of CO_2 released in a pyrolysis at very high temperature. XPS was measured on a SPECS system equipped with a Phoibos 100 hemispherical electron energy analyser. The samples were fixed to the XPS sample-holder with double-sided carbon adhesive tabs. The spectra were acquired at a pressure below 10^{-7} Pa using a monochromatic aluminium X-ray source operating at 14.00 kV and 175 W power. The photo-excited electrons were analysed in constant pass energy mode, using a pass energy of 50 eV for the survey spectra and 10 eV for the high resolution core level spectra. Spectra were recorded at a take-off angle of 90º. CasaXPS software was used for data processing. The compositions in atomic percentage (at%) were determined from the survey spectra (after correction for the mean free-path of the outgoing electrons and the transmission function of the analyser), using the integrated areas of the main XPS peaks of the different elements and their respective sensitivity factors.

2.4 Small and wide angle X-ray scattering

Small and wide-angle X-ray scattering measurements (SAXS and WAXS) were performed on dry and wet carbon samples with incident X-ray energy 17 keV using a CCD camera mounted on the optical bench of beam line BM02 at the European Synchrotron Radiation Facility, Grenoble, France. Three sample-detector distances were employed for each sample: 52.6 cm, 14.5 cm, and 5.7 cm. The samples were held in the same thin-walled, sealed Lindemann glass capillary tubes of diameter 1.5 mm described above. Measurements were made in the wave vector range $6\times10^{-3} \leq q \leq 6$ Å^{-1}, where

$$q = 4\pi/\lambda \sin(\theta/2), \tag{1}$$

λ being the wavelength of the incident radiation and θ the scattering angle. Standard corrections were made for grid distortion, sample transmission and background subtraction, thus taking into account the effects of absorption, including impurities in the sample, and the weak signal from the capillary glass. For each sample-detector distance the values of q were calibrated with silver behenate (AgBeh). At the shortest distance, 5.7 cm, where resolution is lowest, coincidence with the response at 14.5 cm was found by aligning the strong AgBeh reflections lying between 1.38 $Å^{-1}$ and 1.81 $Å^{-1}$. The resulting correction introduced here slightly decreases the values of q in the WAXS region with respect to those reported in ref [22].

The specific surface area, S_X, of the dry samples was calculated from the second moment of the total scattering spectra, and by extrapolating to the limits $q_{min}=10^{-4}$ $Å^{-1}$ and $q_{max}= \infty$, as described in reference [27]. $S_X = S/(V\delta_{av})$, where S is the interfacial area within a volume V in the vicinity of a carbon atom and δ_{av} is the apparent (macroscopic) density of the carbon sample.

2.5 TEM

The morphology of the samples was characterized by a FEI Titan Themis 200 kV spherical aberration (Cs) corrected TEM 0.09 nm HRTEM and 0.16 nm STEM resolution equipped with 4 Thermofischer “Super X G1” EDS detectors. The samples were drop-dried on TEM microgrids coated with an ultrathin carbon layer.

2.6 Solid-state NMR

High-resolution magic angle spinning (MAS) solid-state NMR spectra were recorded on a Varian System spectrometer operating at ^1H frequency 400 MHz with a Chemagnetics 4.0 mm narrow-bore double resonance T_3 probe at 25 °C with spinning rate 10.0 kHz and repetition delay 20 s. A PDMS rubber sample was used as outer chemical shift reference. Samples were transferred into a 4 mm rotor and sealed hermetically with Resolution NMR Sealing System. 256 transients were collected after 20 minutes of temperature equilibration. Background correction of the recorded FID-s was performed by subtraction of the signal from the dry sample, after which it was processed with VNMRJ software and de-convoluted by the DMFIT program. [28]

2.7 Pulsed field gradient NMR

Pulsed field gradient NMR (PFGNMR) yields information on the mobility of the adsorbed water molecules. It measures the decay rate of the spin echo signal due to molecular diffusion as a function of the time difference Δ between two field gradient pulses of intensity *g* and duration δ [29] Measurements were made using a Bruker NMR analyser (mq20) working at 20 MHz, equipped with a temperature-controlled probe and coils that delivered a field gradient pulse of up to *g*=4 T/m.

3 Results and Discussion

3.1 Dry carbons

3.1.1. Morphology

Figure 1 a shows the nitrogen adsorption isotherms at -196 °C on the two samples and the corresponding pore size distributions. CO_2 adsorption data measured at 0 °C (Figure 1b) were used to reveal the ultra-micropore range. For the N_2 adsorption data, QSDFT with slit/cylindrical pore geometry provided the best PSD fit. The figures show that the acidic treatment hardly affected the pore morphology. The samples are highly microporus according to their transitional isotherm of Type I- IV [30] with a narrow H4 type hysteresis loop often found in carbons having mainly micro- and mesopores. In contrast, the water vapor isotherms [22] show the typical convex shape (**Figure S1**). Their initial section, which can be correlated with the O-containing functional groups [2, 4, 10] implies that the oxidation was successful.

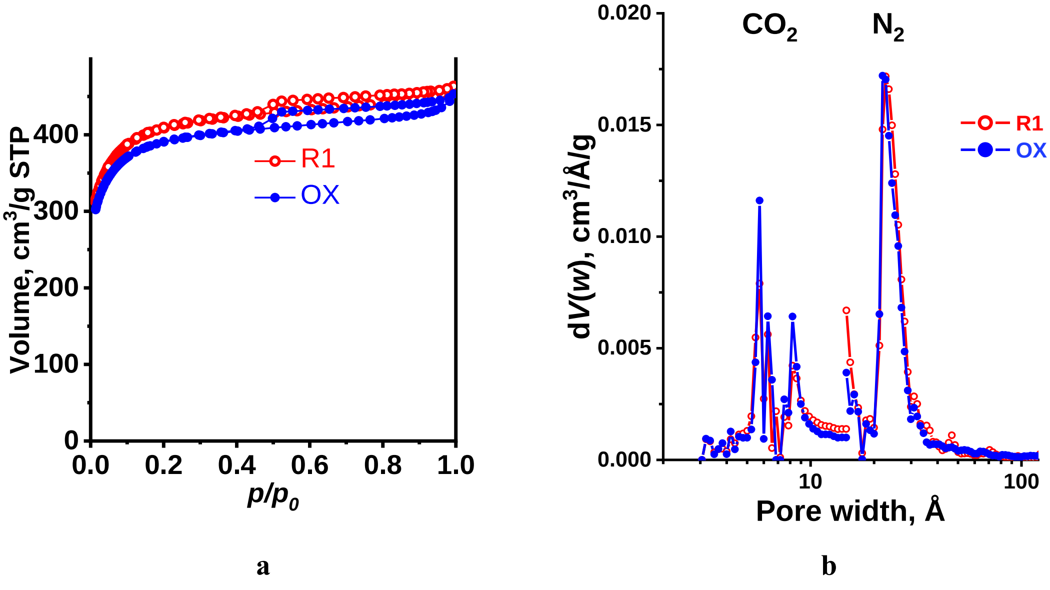

a b

Figure 1 a) Nitrogen adsorption isotherms at – 196 ºC; b) Pore size distribution curves. PSD in the ultramicropore range was deduced from the CO_2 adsorption isotherms (0°C). QSDFT theory with slit/cylindrical geometry was used for PSD from N_2 isotherms. The overwhelming majority of pores accessible to nitrogen lie in the size range 4 - 25 Å.

Table 1 Principal characteristic data* [22]

	R1	OX
S_{BET}, m^2/g	1519	1450
V_{TOT}, cm^3/g	0.72	0.70
$V_{micro,DR}$ cm^3/g	0.61	0.58
$V_{micro,QSDFT}$ cm^3/g	0.4964	0.4773
V_{ultra}, cm^3/g	0.023	0.022
δ_{He}, g/cm^3	2.21	2.10
δ_{av}, g/cm^3	0.854	0.835
S_X, m^2/g	1710	1690

*S_{BET}: apparent surface area from the BET model, V_{TOT}: total pore volume at $p/p_0 \approx 1$, $V_{micro,DR}$ and $V_{micro,QSDFT}$: micropore volume from the DR and QSDFT models, respectively, V_{ultra}: volume of ultramicropores from CO_2 adsorption; d_{ave}: average pore diameter, δ_{He}: density of the carbon matrix measured by helium pycnometry, δ_{av} : apparent (macroscopic) density, S_X: specific surface area from SAXS measurements.

Examination of the TEM micrographs of R1 and OX (**Figure 2**) reveals multiply overlapping turbostratic platelets of size 20-50 nm or greater with nanometric-sized distorted graphitic-like inclusions, [31], and having irregular surface structure.

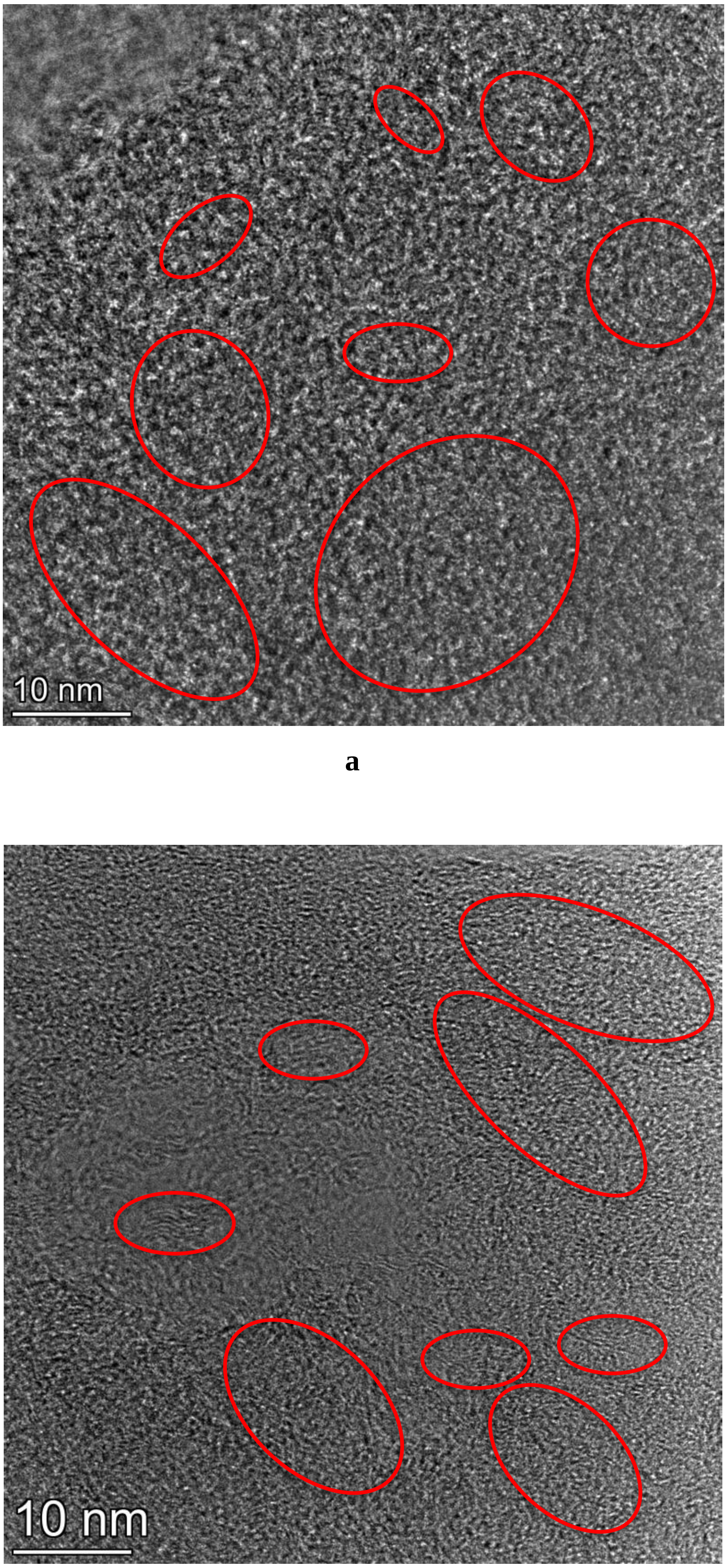

a

b

Figure 2. a) TEM micrographs of dry R1 carbon at high resolution showing overlapping turbostratic fragments***;*** b) TEM micrographs of dry OX carbon at high resolution, revealing

platelet turbostratic fragments with nanometric-sized distorted graphitic inclusions a selection of which is outlined approximately**.** The corresponding FFT images are shown in **Figure S2**.

The WAXS spectra of R1 and OX exhibit three principal broad peaks in the q range explored, labelled p_1, p_2 and p_3, demonstrating that limited order exists in the structure despite the general disordered nature of the samples. To interpret the WAXS spectra it is helpful discuss them by analogy with crystalline graphite [32]. The broad peaks in **Figure 3a** with maxima denoted by vertical arrows are characteristic of a semi-amorphous carbon material composed of nanometre (or greater) sized regions with distorted sheets and corresponding slit-pores of variable size. The principal interatomic distances, which, in crystalline graphite, result in the particularly strong (002) reflection at 1.873 Å^{-1}, are displaced here. The first broad peak at 1.54 Å^{-1}, observed in our samples, implies a wide range of interlayer spacings in the dry carbon, with an average slit-pore size (inter-sheet distance) of about $2\pi/1.54 \approx 4.08$ Å, wider than that in graphite, 3.35 Å. In this partially separated state, loss of correlation between neighbouring planes extinguishes crystallographic reflections of type ($h,k,l \neq 0$). Moreover, the (100) crystalline reflection in graphite at 2.95 Å^{-1} here emerges as a broad peak at 2.84 Å^{-1}, while the (110) peak appears at 4.94 Å^{-1}, instead of 5.10 Å^{-1}. [20, 21] These results indicate that in the dry samples the average interlayer distance between neighbouring graphene sheets is more than 20% greater than in graphite, while the in-plane interatomic spacing is also larger, but to a lesser degree.

The above observations are consistent with the structural model proposed by Oberlin [33]. More recently, the novel Annealed Molecular Dynamics (AMD) simulations based approach by de Tomas et al [34, 35], which was first used for carbide derived carbons, impressively visualizes the disordered 3D graphene network of Norit R1 Extra [36]. Excellent agreement has been found between the isotherms simulated on the structure shown in **Figure 3b** and experimental isotherms of Norit R1 Extra reported in the literature [37].

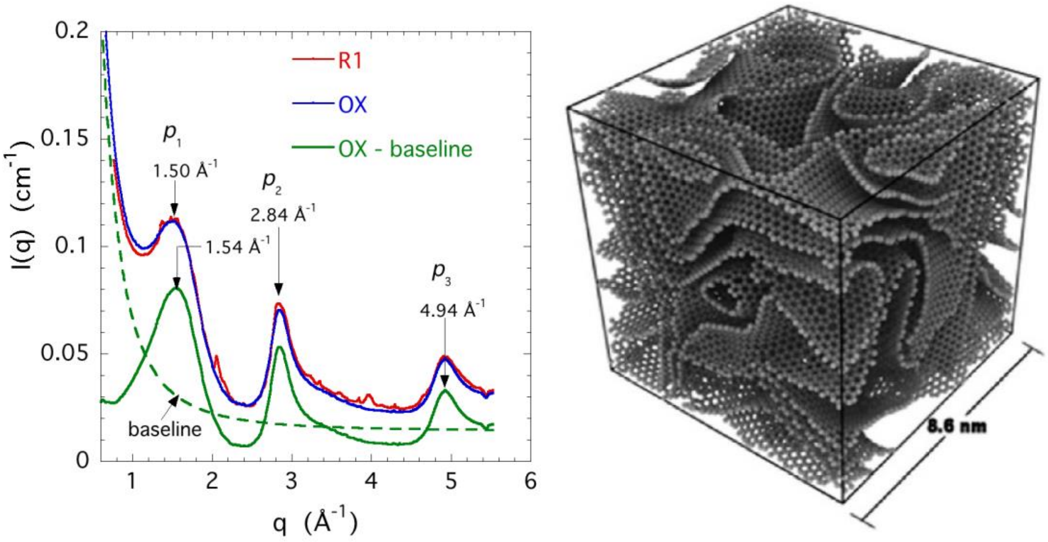

a **b**

Figure 3. a) Wide angle X-ray response of the two dry samples R1 and OX (two upper continuous curves), displaying their three principal broad peaks, p_1, p_2 and p_3. The responses of R1 and OX are almost identical, but R1 (red line) contains a small fraction of foreign crystalline impurities that appear as small irregular sharp peaks above the carbon signal. Absence of these irregular peaks both in OX (blue line) and in the hydrated R1 carbon (Figure 8) implies that these impurities are at least partially water-soluble. NB: the apparent position of the first peak (p1) at 1.50 Å^{-1} is shifted by the overlapping small angle scattering. Subtraction of this baseline (dashed curve) yields a corrected dry OX response (lowest continuous curve) with peak centred at 1.54 Å^{-1}. b) 3D molecular model of the microporous structure of Norit R1 [36, 37], indicating a complex folded sheet structure of the graphene layers. The box-size is 8.6 nm and contains 32,000 carbon atoms [36]

3.1.2 Chemistry

The bulk and surface chemistry of the samples were characterized by several techniques. **Table 2** shows the results of the bulk and XPS analyses. The XPS survey spectra of the samples are displayed in **Figure S3**. The sum of the bulk concentrations did not add up to 100% of the samples. The remaining ash was 5.7 and 4.5 wt% in the R1 and OX sample, respectively. The main components of the R1 ash (from XRF analysis) were sulphur (16 wt%), potassium (7% wt), silicon (9 wt%), calcium (42 wt%) and iron (22 wt%) [22]. These values are similar to data found in other plant based Norit carbons [38].

Table 2 Bulk and surface chemical composition of the Norit samples

Sample	Elemental analysis*						XPS				
	C	O	N	H	S	O/C	C	O	S	Ca	O/C
	at%						at%				

Norit R1	92.6	3.0	0.2	4.0	0.2	0.03	94.6	4.85	0.33	0.22	0.05
Norit OX	87.7	6.3	0.6	5.3	0.1	0.07	93.02	6.81	0.17	-	0.07

* of the non-ash part

The fact that N is detected by elemental analyses but not by XPS may be due either to the presence of this element in the bulk of this sample but not on its surface, or to an error in the elemental analyses. The small difference between XPS O/C ratios (from 5 to 7 oxygen atoms in every 100 carbon) reveals that the oxidation is mild, and – based on the O/C ratios – more significant in the bulk. Comparison of the C 1s regions (**Figure 4a**) confirms the subtlety of the oxidation. The most remarkable is the diminution of the graphitic component, centred at ~284.5 eV, while the amount and relative contribution of the carbons bonded to oxygen, whose signal appears above 286 eV, remains nearly unchanged. No further conclusions were drawn from the C 1s region owing to the small difference between spectra. Comparison of the O 1s region (**Figure 4b**) shows that all kinds of oxygen functionalities increased upon oxidation. The inherently broad O 1s signal, combined with the small chemical shifts for oxygen bonded to carbon atoms, hampers a meaningful deconvolution of this region [39]. Nevertheless, the deconvolution of the O 1s signal and its discussion are shown in **Figure S4.** The amount of all oxygen containing functionalities, apart from O*, increased with the oxidation, with a slight predominance of oxygen singly bonded to carbon, i.e., carbonyl and phenolic groups.

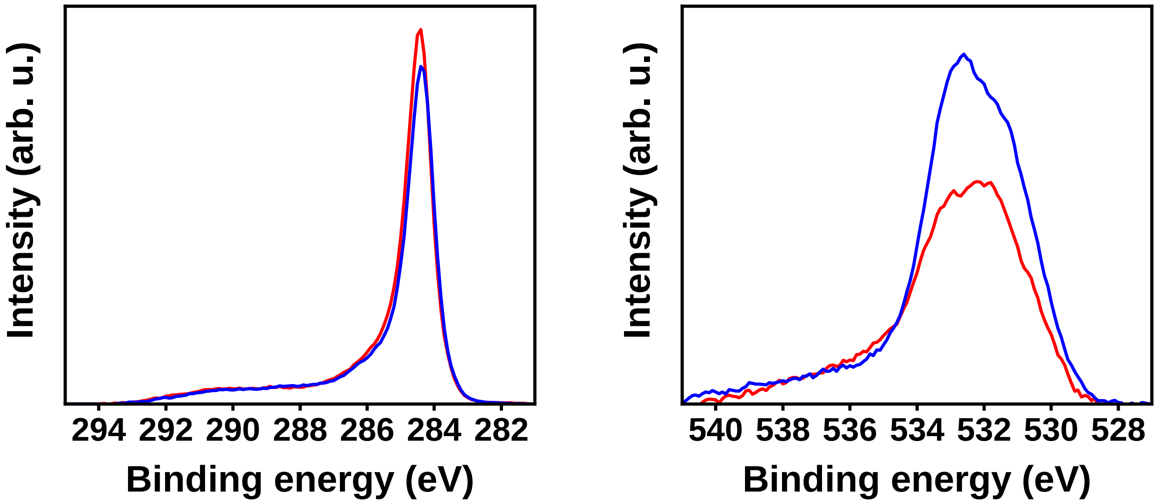

a **b**

Figure 4. Comparison of the background-subtracted high-resolution **(a)** C 1s and **(b)** O 1s core level spectra for R1 (blue) and OX (red)

TG/MS assisted temperature programmed desorption (TPD) is particularly appropriate for characterizing oxygen functional groups in highly porous carbon matrices [40, 41]. CO_2 and CO signals are widely used to identify the O-containing surface groups (**Figure 5**). The increased O-content is reflected in the enhancement of both the CO and CO_2 signals, i.e., the nitric acid oxidation enhanced the population of several different types of O-containing functional groups [40, 41]. Despite the relatively high heating rate used in the TG/MS measurements, the identity of the functional groups contributing to the CO and CO_2 evolution can be deduced from the location of the maxima in the corresponding profiles (**Figure S5**).

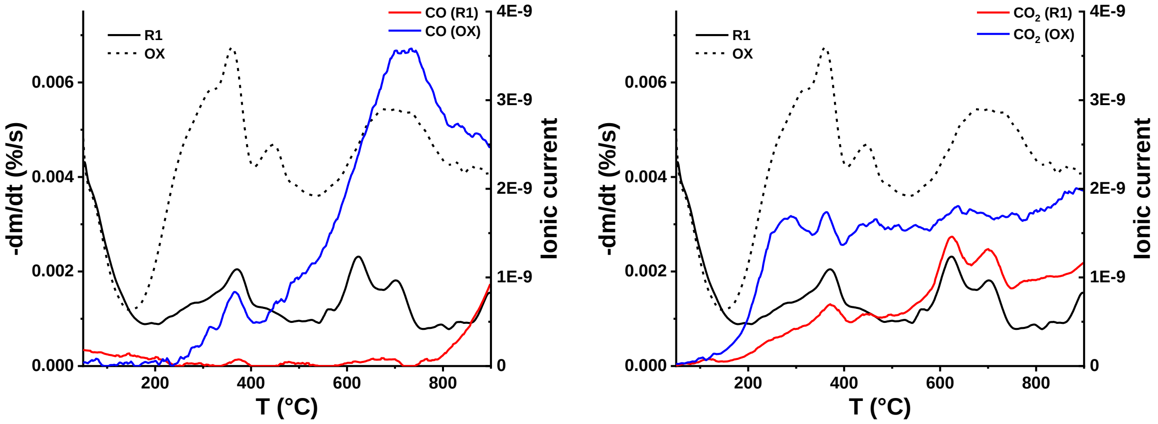

a **b**

Figure 5. CO (M/Z = 28) (a) and CO_2 (M/Z=44) (b) release of the carbon samples from TG/MS analysis

XPS and TG/MS concord in implying that the amount of phenolic and carbonyl groups increases with the oxidation. The enhancement of carboxylic groups is also indicated from the TG/MS but not from the XPS results. Such an “anomaly” was previously observed on highly oxidized carbon materials rich in labile oxygen functionalities, e.g., graphene oxide and reduced graphene oxide [42]. The groups that decompose at 250~300 °C in our TG/MS experiment could be lost during the ultrahigh vacuum treatment preceding the XPS measurement.

3.2 Hydrated carbons

3.2.1 Solid-state NMR

Measurement by high field nuclear magnetic resonance of the proton signal from water adsorbed on the carbons, with magic angle spinning to reduce magnetic dipolar broadening, yields information on the nature of the adsorption sites of the water molecules. In particular, the chemical shift, which is governed by proximity of the water to the delocalized electrons of the aromatic carbon surface. With increasing aromatic character of the site the chemical shift tends to negative values. When the surface is oxidized, however, oxide groups disrupt the delocalised electrons, thus decreasing the aromatic nature of the carbon sites, and making the chemical shift slightly less negative. [43] The resulting ^{1}H spectra from hydrated R1 and OX are shown in **Figures 6a** and **6b** respectively. Each figure displays the total signal (red curve), which is accurately represented by three Gaussian components of differing chemical shift and width. The width and centre of the corresponding components are listed in **Table S1**.

In both R1 and OX the chemical shift is essentially negative. This important finding indicates that the adsorbed water molecules are all located in an aromatic environment, lying close to the carbon matrix. According to Figure 6, the sites in the untreated sample R1 are more strongly aromatic, on average by 1 ppm, than those in the oxidized form OX. This result is consistent with the more polar character of the oxidized surface.

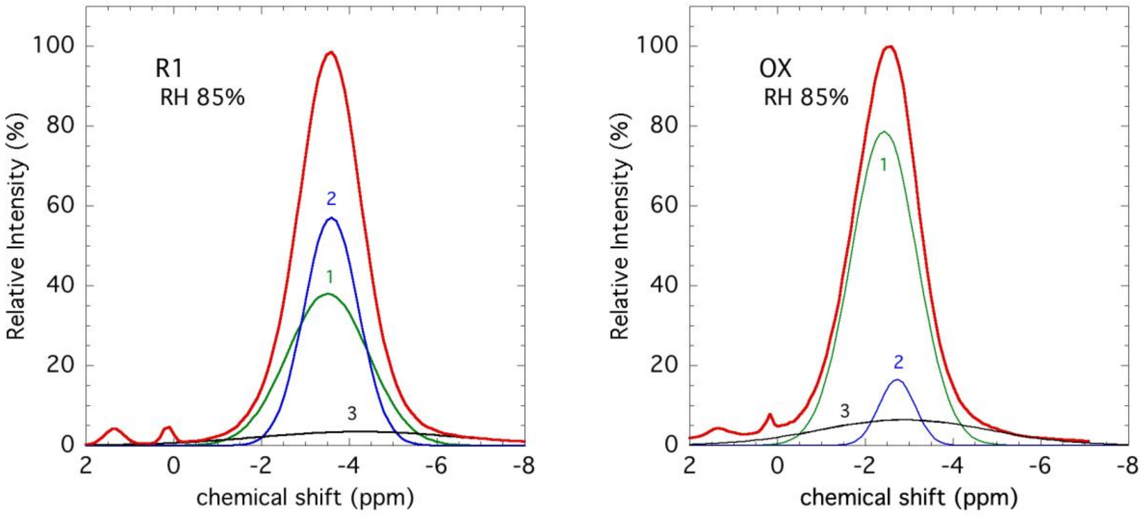

a **b**

Figure 6. High field ^{1}H NMR spectra with magic angle spinning of R1 85% RH (a), OX 85% RH (b), after subtraction of the signal from the dry sample. Red curves are the observed total response; the green, blue and black curves (numbered 1, 2 and 3) are the respective Gaussian components of the decomposition (see Table S1). The small peaks appearing between chemical shift +2 and 0 ppm, extraneous to the carbon sample, stem from the sealant used to close the rotors.

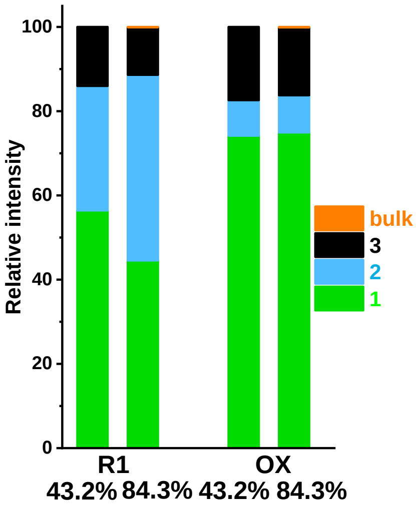

Figure 7. Histogram of integrated intensity of the 3 observed Gaussian components in each distribution of chemical shifts of the adsorbed water molecules in Figure 6. The two samples R1 and OX are shown for two values of RH: 43.2% and 84.3%. Numerical data are listed in **Table S1**. Note: component #4 with chemical shift +4.79 ppm (bulk water) comprises no more than 0.1% of the total, although barely visible in this figure, is excluded from the calculation.

The widths of the distributions in Figure 6 (Table S1) are generally broader than, but of the same order as, the difference in chemical shift between the untreated and the oxidized samples, but component 2 is distinctly narrower than component 1. Similarly to XPS and TG/MS, they indicate a richly varied landscape of sites for the water molecules, among which the distribution of the minority component (#3) is in each case outstandingly broad. It is also noticeable that in each case in Table S1 the proportions of each component are roughly similar. While it is difficult to attribute the various components with certainty, the difference in the width of the components suggests that they correspond to populations in physically different regions. It is reasonable therefore to associate the majority components with locations inside the micropores and small mesopores, since those are the sites that fill first. Table S1 indicates that these molecules are also those with the least (negative) chemical shift, i.e., either farther from an aromatic surface or associated with a polar impurity. Evidence from small angle neutron scattering (SANS) on OX carbons with various ratios of deuterated and protonated water has shown that in wide pores (those detected in the region explored in the lowest *q* region SANS), water molecules form large clusters around a polar group without direct contact with the aromatic surface. [4, 5] The attribution of the three components is however left to the next section.

Although Figures 6-7 yield no information on the mobility of the water molecules, the continuous nature of the chemical shift spectra suggests that energy differences between sites is small and that the molecules are not necessarily rigidly localized. Presence of spinning side-bands of very low intensity (2-4 %), however, indicates a partly mobile nature of the adsorbed water molecules. Furthermore, while the negative chemical shift in Figure 6 demonstrates that the adsorbed molecules are all located within the samples, at high RH (84.3%) a very small fraction (ca 0.1%) of excess water is detected that exhibits the same value of chemical shift, about +4.8 ppm, as bulk water. At high values of RH, some free (or bulk-like) water thus remains condensed on the surface of the carbon.

3.2.2 *WAXS*

Figure 8 shows the effect of adsorbed water on the wide-angle X-ray scattering response of the samples in the range $0.6 \leq q \leq 6$ Å^{-1}. The peaks p1, p2 and p3 of Figure 3 each become increasingly intense. It is notable in Figure 8a that, even at RH 85%, sample R1 still displays visible signs of crystalline impurities.

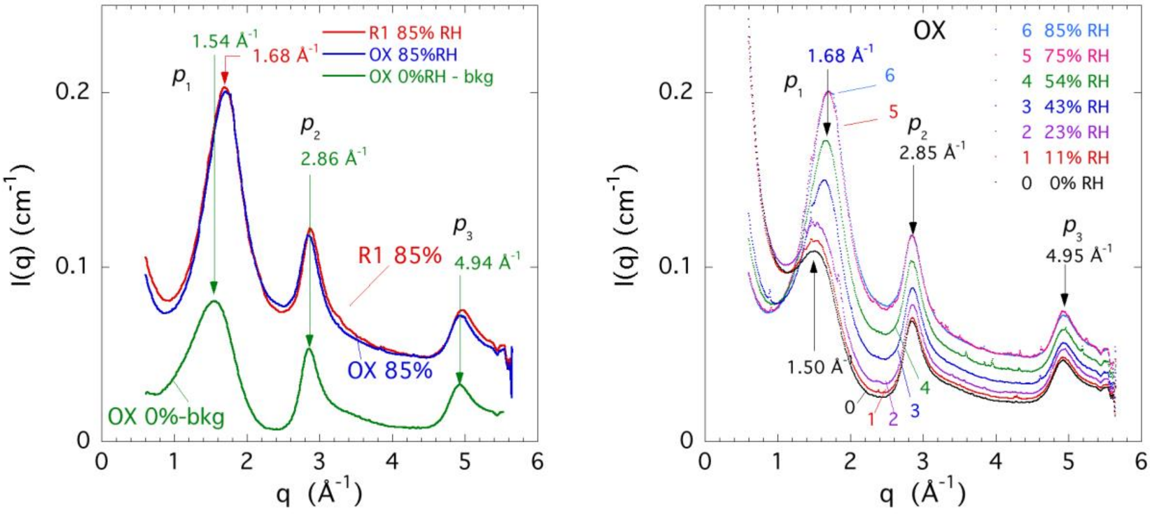

a **b**

Figure 8 a): WAXS intensity of the hydrated (RH=85%) R1 and OX samples (red and blue curves respectively) compared with the corrected dry OX sample (green curve) from Figure 3a; **b**): WAXS response of OX samples as a function of RH, displaying the appearance of a new peak at 1.68 Å^{-1} of increasing intensity, just above the first maximum p_1 at 1.50 Å^{-1} (before background correction) in the dry state. At high RH the effect of SAXS background subtraction on the peak position is negligible.

In crystalline graphite, the interlayer spacing, 3.35 Å, [33] is too narrow for water molecules to enter. In the dry amorphous carbon samples, by contrast, the average interlayer spacing is $2\pi/q_{p1}$=4.08 Å, where according to Figs 3a and 8a, q_{p1} =1.54 Å^{-1} is the most probable interlayer distance. This wider spacing is ample for water molecules to penetrate and attach as a monolayer to either side of the separated graphene sheets. Earlier observations [22] have shown that when either R1 or OX is left in contact with bulk liquid water for a month the volume of the carbon expands by a few per cent. Figure 8b indicates, however, that as the water content increases, the peak positions p2 and p3 remain constant, i.e., the in-plane dimensions of the carbon sheets are invariant. Any swelling at high water content can therefore involve an increase only in the interlayer spacing, i.e., a shift of peak p1 to lower values of q.

At high RH, however, Figure 8 shows that the signal from the water in the first maximum, q_1, in the hydrated samples appears at 1.68 $Å^{-1}$, notably *higher* than that, 1.54 $Å^{-1}$, of the interlayer spacing in the dry carbon state. This peak is therefore unrelated to the interlayer spacing, and originates only from within the adsorbed water itself. It corresponds to an average in-plane intermolecular spacing of about $2\pi/1.68=3.74$ Å. Although, as will be shown, the water molecules are mobile, it is noticeable that the latter distance coincides with the intermolecular spacing in ice Ih, [44] i.e., substantially greater than in bulk water, 3.1 Å. This finding suggests that the density of the adsorbed water layers is lower than in the bulk state. (Note that for convenience we adopt here the convention that spatial separations are defined by the quantity $2\pi/q$, which, although valid in regular crystallographic structures, is only approximate in disordered systems.) By contrast, while the position of the two other prominent peaks in Figure 8b, q_2=2.85 $Å^{-1}$ and q_3= 4.95 $Å^{-1}$, remains unaffected by the presence of adsorbed water, their numerical values are nevertheless significantly lower than in graphite, indicating that interatomic distances in the graphenic planes have increased. The commensurate increase in intensity of these peaks with increasing RH indicates that the water molecules tend to occupy vacant sites on or within the graphitic layers.

These considerations suggest that the first two components in Table S1 stem from water in the regions where the turbostratic graphenic layers of the sample are either narrowly or widely spaced. The weakest signal, with the broadest span of chemical shift, seems likely to come from water adsorbed on the edges of sheets. With respect to swelling of the carbons, we recall here, as reported earlier, [22] that the intensity of peak p1 in sample OX 97%RH (not shown here) is some 15% lower than that in OX 85%RH, in spite of its position being identical. This discrepancy is attributed to swelling of the oxidized sample, which in R1 occurs only in contact with bulk water.

3.2.3 SAXS

Unlike the wide angle X-ray scattering response, in the small angle scattering region (q <1 $Å^{-1}$) the signals from the carbon and the water molecules cannot be reduced to a sum of two terms. The signal is governed instead by the difference in electron density (contrast) between the carbon and the medium present in the pores. The total response can thus yield information on the amount of adsorbed water, as expressed through a pore filling factor $p(q)$ at short distances (i.e., high q), such that the ratio of the signals $u(q)$ between the wet and dry carbon samples is

$$u(q)=I_{wet}(q)/I_{dry}(q)=[\rho_{C}- p(q)\rho_{H2O}]^2/\rho_{C}^2 \qquad (2)$$

where $\rho_C=N_A\delta_{He}/2$ and $\rho_{H2O}=10N_A/18$ electrons/cm^3 are respectively the electron density of the carbon and of water, and for simplicity the density of the adsorbed water is taken to be 1 g/cm^3. Here N_A is Avogadro's number, δ_{He} is the helium density of the carbon, listed in Table 1. Note that the local electron densities δ_{He} are much higher than the corresponding average macroscopic electron densities, δ_{av}, also listed in Table 1.

The general features of the small angle scattering responses are displayed in **Figure 9**, both for the R1 and the OX samples, for different values of RH. As described in ref [22], in the highest q region of small angle scattering (Fig 9, Zone B) the intensity $I(q)$ is expected to vary as

$$I(q) = K/q^4 + b, \qquad (3)$$

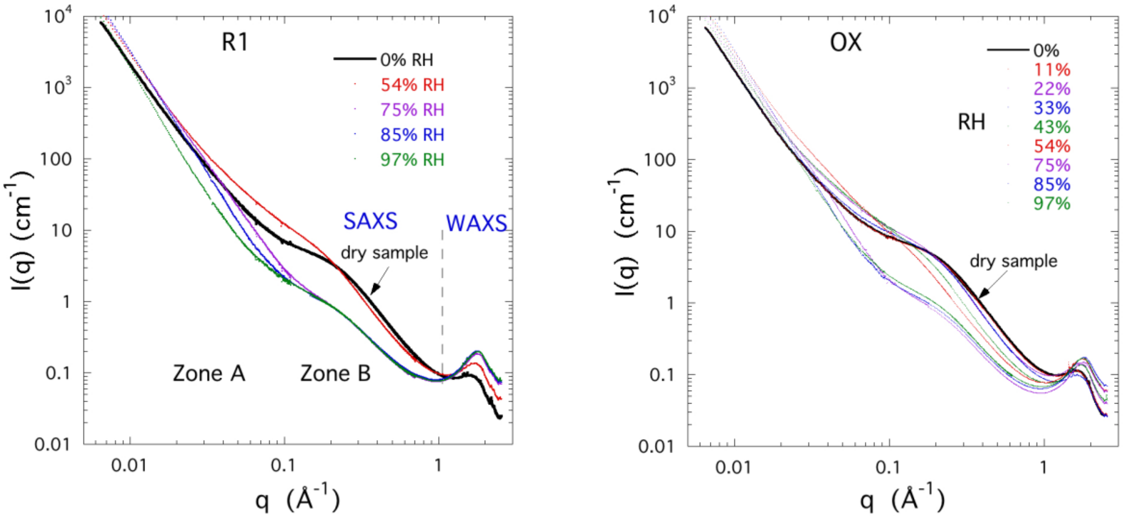

a **b**

Figure 9. SAXS response of the carbon samples at different values of relative humidity RH. In a) the dashed vertical line indicates the approximate border between SAXS and WAXS regions.

where K is the “final slope” due to scattering by the interface between two continuous media [45] and the constant b is sometimes attributed to the atomic disorder in the sample.[46] In this limit, the factor $p(q)$ describes the filling of the smallest pores

$$p_{micro} = \rho_{C}\,[1- (K/K_{\mathrm{dry}})^{1/2}]/\rho_{\mathrm{H2O}}, \tag{4}$$

Here K and K_{dry} are the final slopes of the q^{-4} behaviour in the high q range of the wet and dry SAXS response. [22] As an example, **Figure 10** shows the scattering responses of the dry and humid R1 and OX samples in the high q region, using an alternative representation of Eq. 3, $I(q)q^4$ *vs* q^4, such that the intercept at q^4=0 yields the value of K, and the slope defines b. Similar behaviour is found for the OX samples.

In the SAXS region of Figure 9, in both R1 and OX, the reduction in contrast of the carbon due to the water in the small pores (Fig 9, Zone B) reduces the scattering intensity with respect to the dry material, such that the ratio $u(q)=I_{wet}(q)/I_{dry}(q)<1$. At very small values of q (Figure 9, Zone A), however, where the spatial distances $2\pi/q$ sampled become large, the response is determined by the contrast between water-containing regions in the carbon matrix, in which the total electron density is higher, and the dry regions, where it is lower. The ratio $u(q)$ can there exceed 1.

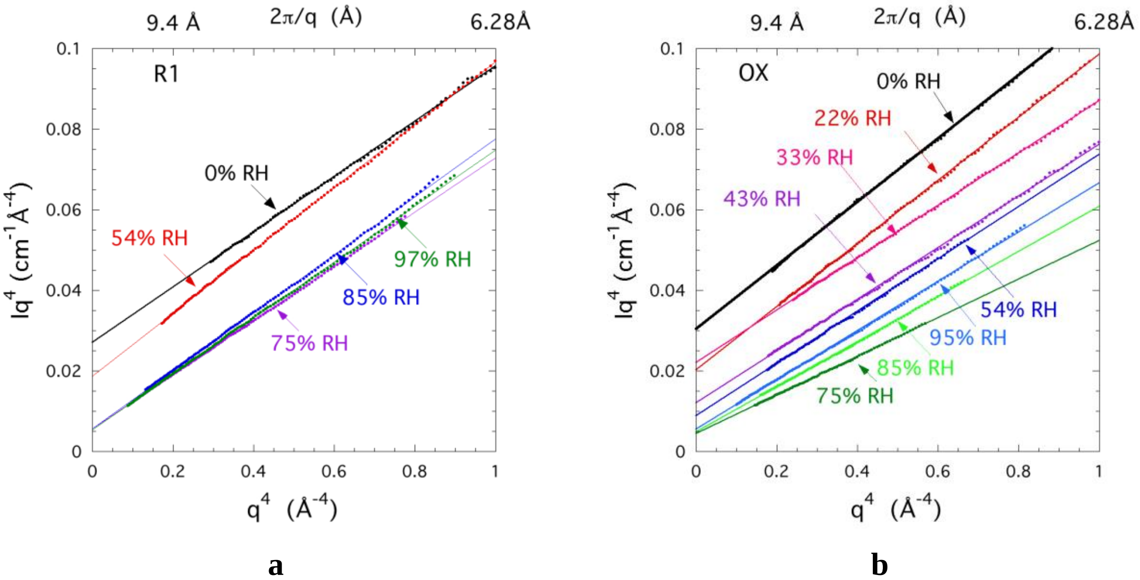

a **b**

Figure 10. Intensity of a) R1 and b) OX samples in the high q SAXS region, plotted in the representation $I(q)q^4$ vs q^4, at different values of RH. The intercept at q^4=0 defines the “final slope” K, [44] and the slope of the lines in this representation determines the so-called atomic disorder parameter b. [46] The upper axis indicates the range of distances $2\pi/q$ explored in

these measurements. It is notable that at higher values of q^4 the response of the water-containing samples deviates from Eq.3: unlike the carbon substrate, the bulky water molecules do not form a smooth surface at high resolution. This deviation marks the onset of the WAXS response of the adsorbed water molecules.

To allow the notion of filling factor $p(q)$ employed in Eq. 2 to describe the scattering behaviour both in the high and intermediate q SAXS regions, it is helpful to redefine the intensity ratio $u(q)$ as

$$u(q)=[I_{wet}(q)-b_{wet}]/[I_{dry}(q)-b_{dry}] \tag{5}$$

It is notable that this subtraction of the measured atomic disorder factors b_{wet} and b_{dry} from the respective total intensities in Eq. 5 removes the particulate nature from the SAXS responses and treats the components as ideal continuous media.

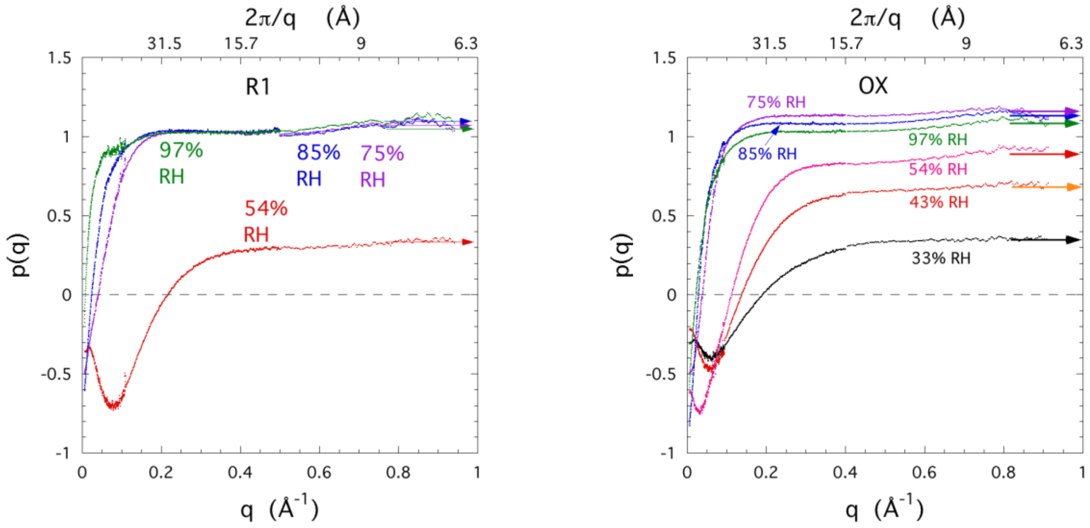

a **b**

Figure 11. Filling factor $p(q)$, with $u(q)$ defined by Eq. 6, for different degrees of RH in samples R1 (a) and OX (b). The arrows on the right-hand side are the values of p_{micro} calculated from Eq. 4. The upper scale indicates the approximate size $d=2\pi/q$ of the corresponding pores.

With the expression for $u(q)$ defined by Eq. 5, the pore filling factor $p(q)$,

$$p(q)= \rho_C[1-(u(q))^{0.5}]/\rho_{H2O} \tag{6}$$

displayed in **Figure 11**, shows that as q tends to 1 the curves converge towards the value predicted by the final slope of Eq. 4. The curves also show that the micropore and small intermediate pore regions (0.3 Å^{-1} $<q\leq1$ Å^{-1}) are the first recipients of the adsorbed water, which appears to be in agreement with the size distribution of the pores observed by nitrogen adsorption. At high relative humidity there is also a tendency for the value of p_{micro} to be

slightly in excess of 1. Although this observation could be interpreted as the density of the water in the micropores being greater than that of bulk water, it is nonetheless more likely that the hydrophobic character of the aromatic carbon atoms prevents them from being tightly surrounded by the water molecules, consequently reducing their effective electron density below that measured by helium pycnometry [47]. This explanation is not necessarily inconsistent with the density of the adsorbed water being simultaneously slightly lower than in the bulk state, as mentioned in Section 3.2.2.

At low q in Figure 11, by contrast, $p(q)$ decreases, even turning negative. In this region $p(q)$ loses the physical meaning of a pore filling factor. Because the sampling size in a scattering observation is determined by $2\pi/q$, the intensity ratio $u(q)$ at low q now measures the ratio of the difference in the square of the electronic density at increasingly large spatial scales, i.e., between water-containing regions in the carbon matrix and their surroundings, composed of carbon and empty pores. In the latter regions the electronic density ρ_C is no longer that of the dense carbon structure $N_A\delta_{He}/2$ but its large-scale value, $\rho_C=N_A\delta_{av}/2$. The cross-over point q_c, at which $p(q)$ in Eq. 2 becomes negative, is an indication of the size of the water clusters in the water filled regions. **Figure 12** reveals this behaviour more clearly by plotting $u(q)$ vs q on a logarithmic scale, thus expanding the low q range.

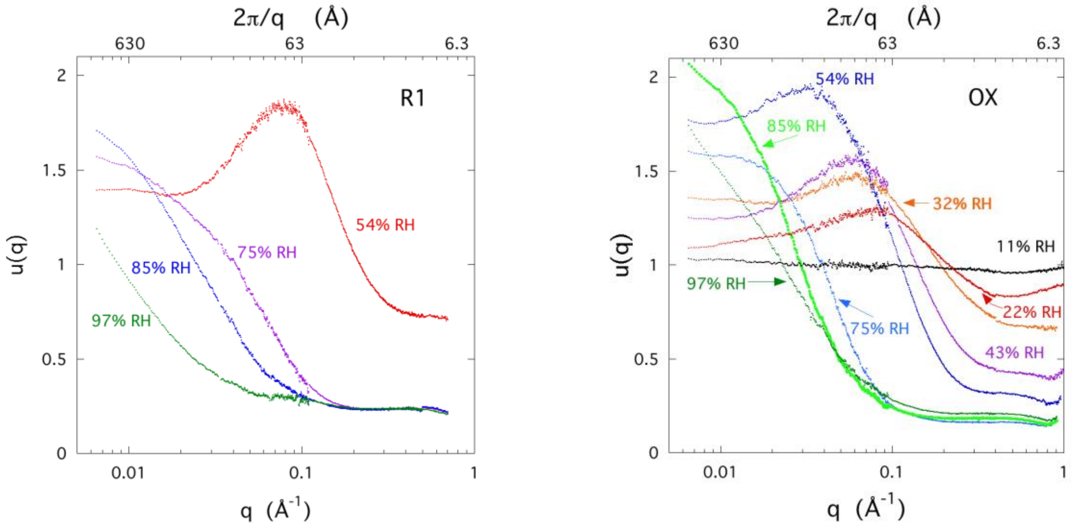

a **b**

Figure 12. Plot of intensity ratio $u(q)=[I_{wet}(q)-b_{wet}]/[I_{dry}(q)-b_{dry}]$ on a semi-logarithmic scale, showing inter-cluster correlation peaks at low relative humidity, and the scattering response of the larger clusters that develop at high RH: a) R1, b) OX. At the lowest value of RH, sample OX 11% RH displays a shallow minimum around $q\approx0.5$ Å^{-1} corresponding to the small amount of water adsorbed, but no clearly discernable correlation peak in the whole q range explored. As in Figure 11, the upper scale indicates the distance $d=2\pi/q$ that corresponds to q.

The appearance of distinct peaks in $u(q)$ in Figure 12 is the signature of spatial correlation between different water clusters, where the maximum at q_{max} defines the characteristic separation distance between neighbouring regions of high water concentration. The distances $2\pi/q_{max}$ in Figure 12 vary from about 80 Å in R1 at 54% RH to almost 200 Å in OX at 54% RH. As the relative humidity increases the cluster sizes also increase, in such a way that correlation between smaller clusters becomes less intense and is lost, while that between larger clusters becomes dominant. This indicates the range in the carbon slit pores over which the carbon substrate is sufficiently continuous to maintain ordered contact within the water clusters. The existence of such clusters has previously been proposed by Kaneko et al. [48, 49, 50]

In the lower q region, $q < 0.1$ Å^{-1}, the scattered intensity from both dry samples R1 and OX develops into a power law of the form $I_{\mathrm{dry}}(q) \propto q^{-n}$, where $n \approx 3.1$. This exponent, close to 3, is the signature of a disordered arrangement of the carbon atoms in which the scattered intensity is simply proportional to the number of carbon atoms in the sample volume explored. In this q region the power law slope differs significantly from -4, and is therefore not attributable to surface scattering from the foreign impurities mentioned in Fig.3 and in Section 3.1.2 [45]. When water molecules are also present, clusters that form contribute extra scattering, such that the total intensity $I(q)$ from the scattering volume is proportional to [45]

$$I(q) = \int \mathrm{d}\mathbf{r}_{\mathrm{j}} \int \mathrm{d}\mathbf{r}_{\mathrm{k}} \rho(\mathbf{r}_{\mathrm{j}}) \rho(\mathbf{r}_{\mathrm{k}}) \exp\left[i\mathbf{q}.(\mathbf{r}_{\mathrm{j}} - \mathbf{r}_{\mathrm{k}}) \right], \tag{7}$$

where $\rho(\mathbf{r}_{\mathbf{j}})$ is the electron density of the sample at position $\mathbf{r}_{\mathrm{j}}$, and similarly $\rho(\mathbf{r}_{\mathrm{k}})$ for the sample at position $\mathbf{r}_{\mathrm{k}}$. The integrations with respect to $\mathrm{d}\mathbf{r}_{\mathrm{j}}$ and $\mathrm{d}\mathbf{r}_{\mathrm{k}}$ are both to be performed over the whole of the illuminated volume. Scattering from identical positions $\mathbf{r}_{\mathrm{j}} = \mathbf{r}_{\mathrm{k}}$ is thus independent of q. The immense majority of scattering however comes from atoms at different positions $\mathbf{r}_{\mathrm{j}} \neq \mathbf{r}_{\mathrm{k}}$. Adsorbed water molecules belonging to a small cluster give rise to scattering over a wide range of q, while that from different clusters, whenever a preferred distance occurs between them, gives rise to increased scattering, i.e., a correlation peak, at the value of q corresponding to their separation. With increasing size of water clusters their distance of separation ($\mathbf{r}_{\mathrm{j}} - \mathbf{r}_{\mathrm{k}}$) must also increase, with the result that the correlation peak increases in intensity and, according to Equation 7, its position q must correspondingly decrease. At values of q lower than the peak the spatial correlation is lost and the ratio $I_{\mathrm{wet}}(q)/I_{\mathrm{dry}}(q)$ decreases to a value closer to, but, owing to the water content, greater than unity.

The data of Figure 12 also provide a means to estimate a radius of gyration R_G of the water clusters. In **Figure 13** we adopt the Guinier representation log($I(q)$) vs q^2, together with the assumption that at $q>q_{\max}$, i.e., immediately above the position of the peak maximum, the slope of the resulting exponential fit in the range $qR_G<1$ is equal to $R_G^2/3$. [45]

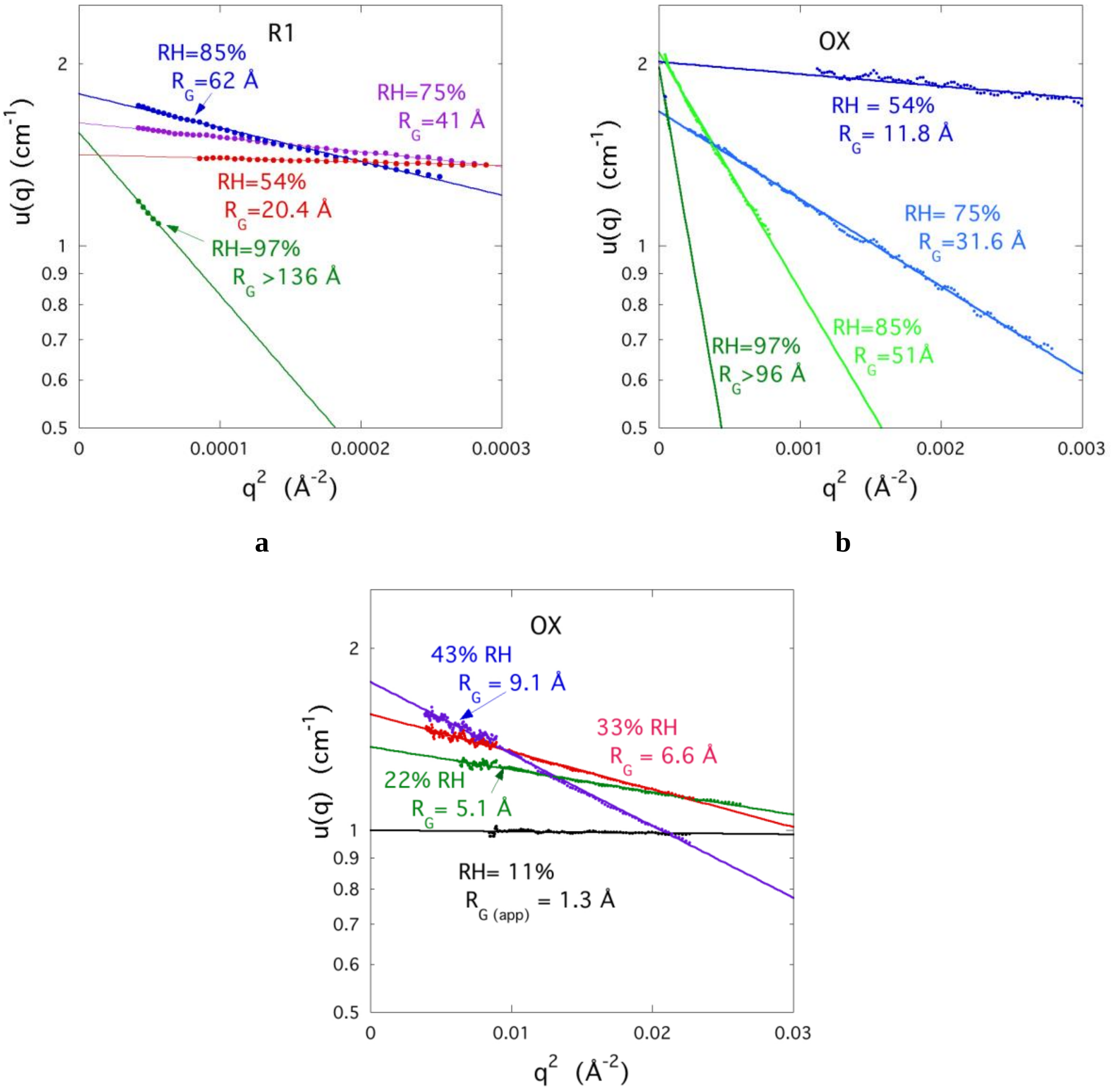

a

b

c

Figure 13. Intensity ratio $u(q)$ in the Guinier representation log($u(q)$) vs q^2: a) R1, (b) OX, in the higher relative humidity range, c) OX in the lower relative humidity range. The slope of the lines is $R_G^2/3$. OX 75% RH exhibits a weak downwards curvature at low q, suggesting a correlation peak beyond the lowest measured value of q, i.e. $2\pi/q_{max}$ > 1000 Å. In a) the data are displayed on an expanded scale, showing that, except for RH=97%, the Guinier condition qR_G <1 is met. [45]

The above findings are summarised schematically in Figure 14a, where the apparent radius of gyration of the clusters, deduced from the high-q side of the correlation peak according to the Guinier approximation $I(q) \propto \exp(-q^2R_G^2/3)$, is plotted as a function of RH. It is notable that, apart from their size R_G, these measurements provide little information on the *shape* of the clusters. With increasing RH, at q<0.015 Å^{-1} the power law slope n of the scattered intensity $I(q) \propto q^{-n}$, increases in both samples (in R1 from 3.1 at 11%RH to 3.7 at 97%RH, and in OX from 3.2 to 3.6). This is consistent with the increasing surface area occupied by the adsorbed water on the graphene layers. Figure 14a shows that apart from at low RH, the RH dependence of R_G is similar in samples R1 and in OX, but slightly larger in R1. It also indicates that at the lowest value of RH, even in sample OX, cluster formation has not yet been able to develop. In this case, the apparent value of R_G is the size of a single molecule. In R1 the first measurable signal is at 54% RH, where cluster formation suddenly appears, and the clusters rapidly spread. As a consequence, in R1 the size of the clusters becomes so great that the correlation peak is shifted beyond the detection range of the present measurements. This is why in Figure 14b no data is recorded for sample R1 only at RH = 54%. This implies that surface chemistry of the substrate plays a role not only in the early stages of cluster formation at low RH, but also at high RH. At low RH polar sites initiate that cluster formation, while at high RH the hydrophobic surface promotes coalescence of the clusters.

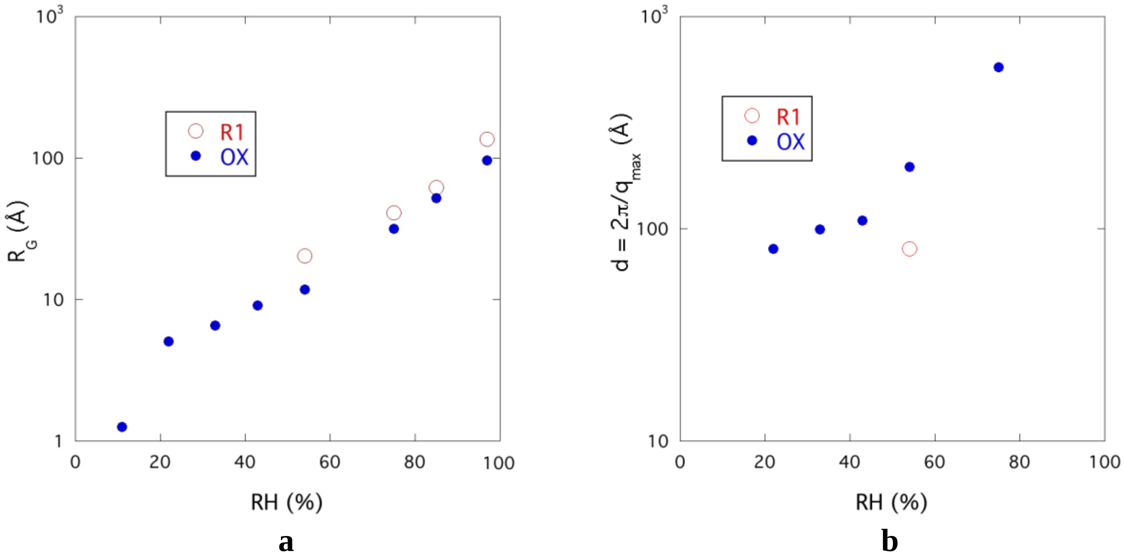

a **b**

Figure 14: Dependence on relative humidity RH of a) the radius of gyration of the clusters of adsorbed water; b) the correlation peak separation $d=2\pi/q_{max}$ on RH in the carbons R1 (open circles) and OX (full symbols), where q_{max} is the correlation peak position in Å^{-1}. At high RH q_{max} lies below the smallest q value explored in these measurements.

3.2.4 Molecular mobility

All the above observations provide information on the *average* positions of the adsorbed water molecules. Apart from the spinning side-bands seen in solid-state NMR, little can be inferred as to whether the water molecules are in a partially frozen or a liquid state, and, if the latter, on their residence time at each site. Such information is however accessible by the use of pulsed field gradient NMR (PFGNMR). As described above in Section 2.8, this technique measures the decay rate of the spin echo signal from the protons in the water molecule as a function of the product Δq^2, where Δ is the time difference between two field-gradient pulses, of intensity g and duration δ, and the effective wave number is $q=\gamma\delta g$, where γ is the gyromagnetic ratio of the protons. [29] The findings are displayed in **Figure 15**.

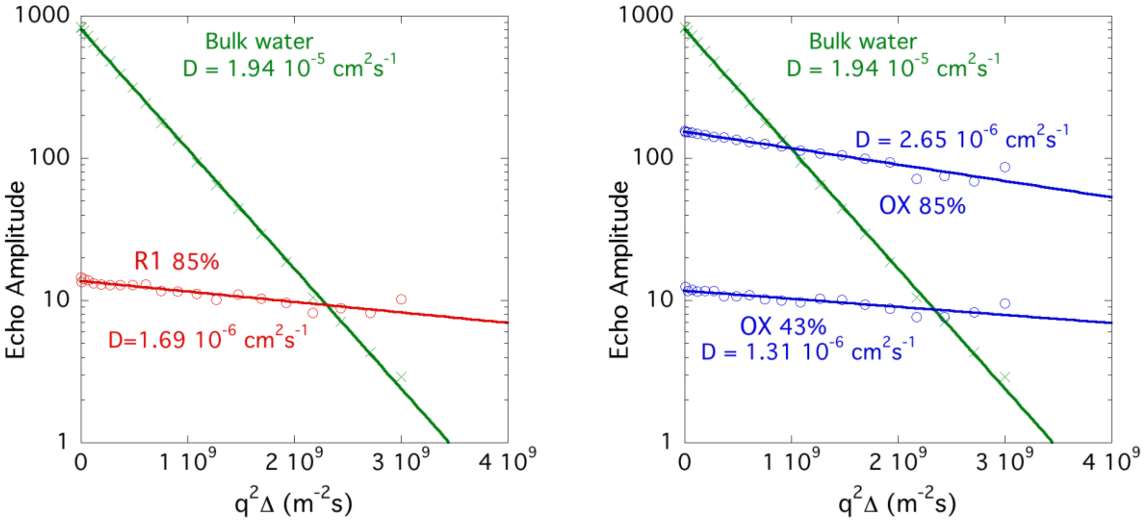

a **b**

Figure 15. Pulsed field gradient NMR measurements at 20 MHz of diffusion of water adsorbed on a) R1 at 85% RH, and b) OX samples at RH 85% and 43% at 20 ºC, compared with bulk water (green data points). The lines are single exponential fits. The signal from sample R1 at RH 43%, although non-zero, was too small to be measurable. The effective transfer wave number is defined as $q=\gamma\delta g$, where γ is the gyromagnetic ratio of the protons, δ is the duration of the gradient pulse, and g is the intensity of the applied magnetic field gradient pulse; Δ is the separation between the two pulses.[29] The slope of the lines in this semi-logarithmic representation yields the translational diffusion coefficient D of the water molecules.

The measured translational diffusion coefficient D in the 85% RH OX sample, 2.65×10^{-6} cm^2s^{-1} at 20 ºC is about an order of magnitude smaller than that measured for bulk water at the same temperature, approximately 1.94×10^{-5} cm^2s^{-1}. On taking into account the relative volume of carbon particles in the sample tube and that of water adsorbed, the signal amplitude indicates that roughly 70% of water molecules in this sample are mobile. In the same sample with 43% RH, however, the diffusion coefficient reduces by half to 1.31×10^{-6} cm^2s^{-1} and the fraction of mobile molecules falls to 7%. In R1 at RH 85% the value of D is 30% lower than in OX, indicating that the residence time between site jumps is longer and the molecules are accordingly more restricted, a result that is consistent with the more strongly negative chemical shift. Moreover, the amplitude of the signal in this case indicates that only about 8% of the water molecules are engaged in this diffusion process. This does not mean however that the other molecules are static, since in the range of $q^2\Delta$ explored, slow diffusion rates are masked by the faster processes. As in the case of the WAXS measurements, in these PFGNMR measurements the signal from sample R1 43% RH was too small to be measurable (an observation consistent with variations experienced among several nominally equivalent samples). These findings suggest that the molecules adsorbed at low RH, i.e., those involved in the initial adsorption process, are more tightly constrained. It seems likely, however, that the increased mobility measured at high relative humidity is a consequence of the increasing size of the water clusters observed here, as proposed by Kaneko et al. [48, 49, 50].

The transverse relaxation time T_2 of the nuclear magnetisation also depends markedly on the degree of hydration: in OX at 85% RH, T_2 = 8.94 ms, while at 43% RH, T_2 = 1.19 ms; in R1 85% RH T_2= 5.09±0.06 ms. The variation of D and T_2 (both of which are inversely related to the residence time of the molecules on each site) with increasing hydration shows that the adsorbed water molecules increase their translational and rotational degrees of freedom. Measurements in bulk water, by contrast, yielded T_2= 232 ms. For convenience, a small amount of copper sulfate solution was added to the ‘bulk water’ sample in order to shorten the relaxation time T_1.

The PFGNMR measurements, which indicate values for the diffusion coefficient D of the order of 10^{-6} cm^2s^{-1}, are consistent with the volumetric water uptake findings, according to which the Hydrosorb water adsorption by the millimetre-sized carbon granules is complete within a period of a few hours ($\tau \approx 1$ mm^2/D). In reference [22] however, a much slower but more extensive uptake was observed by WAXS measurements on both R1 and OX, as well as by gravimetric measurements in R1, revealing a characteristic time of several weeks. This finding implies the existence of internal diffusion processes that are more than an order of magnitude slower than those measured here, probably involving infiltration of the narrowest interlayer spaces.

4 Conclusions

This article brings new observations as well as re-examining previous measurements on the disposition and mobility of water molecules adsorbed in an activated carbon under two different surface chemistry conditions. The two specimens studied were an as-received commercial carbon (R1), and the same carbon after oxidation in concentrated nitric acid (OX). HRTEM images of the dry samples and the corresponding wide-angle X-ray results are mutually consistent, indicating an irregular interleaved arrangement of turbostratic graphene-like layers with a broad range of interlayer spacing and an average value of about 4.1 Å. The widths of the high field NMR response of the adsorbed water are also broad, showing that the landscape of adsorption sites is extremely heterogeneous. All adsorbed water molecules display a negative chemical shift and are thus located close to an aromatic surface. At high relative humidity, however, a tiny fraction of the water (0.01%) displays the chemical shift characteristic of free bulk water (about +4.8 ppm). An important new observation is that the water molecules are adsorbed on both surfaces of the resulting graphene sheets, with an average in-plane spacing of about 3.74 Å, notably larger than in bulk water. The greater intermolecular separation in the adsorbed water than in bulk water is attributed to its practically two-dimensional distribution. No crystalline structure in the adsorbed water layers is observed. Small angle X-ray scattering measurements at low transfer momentum reveal another novel result: water clusters that develop in the carbon matrix display strong mutual spatial correlation, over distances that increase with increasing amount of adsorbed water. At low RH, however, cluster formation does not occur. The translational diffusion coefficients *D* of the adsorbed water, measured by pulsed field NMR, are an order of magnitude smaller than in bulk water at the same temperature (20 ºC), with *D* diminishing further at low relative hydration. These values are consistent with the volumetric uptake rate observed in the water vapour isotherms. Previously observed overall uptake of water vapour spanning several weeks, however, points to the existence of another diffusion process that is more than two orders of magnitude slower, which could correspond to the penetration of water molecules into confined locations.

More generally, our findings appear to be consistent with the current consensus that water adsorption in amorphous carbon is mediated by the coalescence of water clusters that are formed at strongly attractive sites, such as functional groups, and grow with increasing RH [17].

5 Acknowledgments

We warmly thank Gy. Bosznai at BME and Niels Blanc of the ESRF for their invaluable technical assistance and access to data. Access both to the BM2 beam line at the European Synchrotron Radiation Facility as well as to the Bruker mq20 NMR instrument at the Institut Laue-Langevin, Grenoble is gratefully acknowledged. This work is part of the project no. TKP - 9 - 8/PALY - 2021, which has been implemented with the support provided by the

Ministry of Culture and Innovation of Hungary from the National Research, Development and Innovation Fund, financed under the TKP2021 - EGA funding scheme. Z. Sebestyén is grateful for the support of the Bolyai János research fellowship."

References

[1] M.M. Dubinin, Water vapor adsorption and the microporous structures of carbonaceous adsorbents, Carbon 18 (1980) 355–364. https://doi.org/10.1016/0008-6223(80)90007-X.

[2] R.S. Vartapetyan, A.M. Voloshchuk, Adsorption mechanism of water molecules on carbon adsorbents, Usp. Khim. 64 (1995) 1055–1072. https://doi.org/10.1070/RC1995v064n11ABEH000189

[3] D. Mowla, D.D. Do, K. Kaneko, Adsorption of water vapour on activated carbon, Chem. Phys. Carbon 28. (2003) 230–262.

[4] A. Tóth, K. László, Water Adsorption by Carbons. Hydrophobicity and Hydrophilicity, Novel Carbon Adsorbents Chapter 5 (2012) 147−171. https://doi.org/10.1016/B978-0-08-097744-7.00005-3

[5] K. László, B. Demé, O. Czakkel, E. Geissler, Incompatible Liquids in Confined Conditions. J. Phys. Chem. C 118 (2014) 23723−23727. https://doi.org/10.1021/jp506100e

[6] A. Metrane, A. Delhali, M. Ouikhalfan, A.H. Assen, Y. Belmabkhout, Water Vapor Adsorption by Porous Materials: From Chemistry to Practical Applications. J. Chem. Eng. Data 67 (2022) 1617−1653. https://doi.org/10.1021/acs.jced.2c00145

[7] L. Liu, S. Tan, T. Horikawa, D.D. Do, D. Nicholson, J. Liu, Water Adsorption on Carbon - a Review. Adv. Colloid Interface Sci. 250 (2017) 64−78. https://doi.org/10.1016/j.cis.2017.10.002

[8] T.J. Bandosz, Revealing the impact of small pores in oxygen reduction on carbon electrocatalysts: A journey through recent findings. Carbon, 2022, 188, 289-304. DOI: 10.1016/j.carbon.2021.11.071

[9] Fa Yang, Xianyin Ma, Wen-Bin Cai, Ping Song, Weilin Xu, Nature of Oxygen-Containing Groups on Carbon for High-Efficiency Electrocatalytic CO2 Reduction Reaction. J. Am. Chem. Soc. 2019, 141, 51, 20451–20459. https://doi.org/10.1021/jacs.9b11123

[10] P. Lodewyckx, E. Raymundo-Piñero, M. Vaclavikova, I. Berezovska, M. Thommes, F. Béguin, G. Dobos, Suggested improvements in the parameters used for describing the low relative pressure region of the water vapour isotherms of activated carbons, Carbon 60 (2013) 556−558. https://doi.org/10.1016/j.carbon.2013.04.006

[11] M. Kéri, D. Nyul, K. László, L. Novák, I. Bányai, Interaction of Resorcinol-Formaldehyde Carbon Aerogels with Water: A Comprehensive NMR Study, Carbon 189 (2022) 57−70. https://doi.org/10.1016/j.carbon.2021.12.045

[12] T. Iiyama, K. Nishikawa, T. Suzuki, K. Kaneko, Study of the structure of a water molecular assembly in a hydrophobic nanospace at low temperature with in situ X-ray diffraction, Chem. Phys. Lett. 274 (1997) 152–158. https://doi.org/10.1016/S0009-2614(97)00664-7

[13] Y. Zeng, H. Xu, T. Horikawa, D.D. Do, D. Nicholson, Henry Constant of Water Adsorption on Functionalized Graphite: Importance of the Potential Models of Water and Functional Group, J. Phys. Chem. C 122 (2018) 24171−24181. https://doi.org/10.1021/acs.jpcc.8b08036

[14] L. Liu, W. Zeng, S. (J.) Tan, M. Liu, D. D. Do, Microscopic insights into water adsorption in carbon nanopores – the role of acidic and basic functional groups and their configurations. Phys. Chem. Chem. Phys., 2021, 23, 18369. DOI: 10.1039/d1cp02308j

[15] R. Raj, S. C. Maroo, E. N. Wang, Wettability of Graphene. Nano Lett. 2013, 13, 4, 1509–1515. https://doi.org/10.1021/nl304647t

[16] R.R. Nair, H.A. Wu, P.N. Jayaram, I.V. Grigorieva, A.K. Geim, Unimpeded Permeation of Water Through Helium-Leak–Tight Graphene-Based Membranes, Science 335(6067) (2012) 442−444. https://doi.org/10.1126/science.1211694

[17] E. Z. Pina-Salazar, K. Kaneko, Adsorption of water vapor on mesoporosity-controlled single wall carbon nanohorn. Colloids and Interface Science Communications 5 (2015) 8-11. https://doi.org/10.1016/j.colcom.2015.05.002

[18] T. Iiyama, K. Nishikawa, T. Otowa, K. Kaneko, An Ordered Water Molecular Assembly Structure in a Slit-Shaped Carbon Nanospace, J. Phys. Chem. 99 (1995) 10075−10076. https://doi.org/10.1021/j100025a004

[19] M. Bellissent-Funel, R. Sridi-Dorbez, L. Bosio, X-ray and neutron scattering studies of the structure of water at a hydrophobic surface, J. Chem. Phys. 104 (1996) 10023–10029. https://doi.org/10.1063/1.471728

[20] T. Ohba, H. Kanoh, K. Kaneko, Affinity Transformation from Hydrophilicity to Hydrophobicity of Water Molecules on the Basis of Adsorption of Water in Graphitic Nanopores, J. Am. Chem. Soc. 126 (2004) 1560−1562. https://doi.org/10.1021/ja038842w

[21] Y. Sugiyama, R. Futamura, T. Iiyama, Ice-like Structure of Water Confined in Hydrophobic Sub-nanometer Spaces at Room Temperature, Chem. Lett. 51(7) (2022) 760−764. https://doi.org/10.1246/cl.220203

[22] K. László, O. Czakkel, G. Dobos, P. Lodewyckx, C. Rochas, E. Geissler, Water vapour adsorption in highly porous carbons as seen by small and wide angle X-ray scattering, Carbon 48 (2010) 1038 –1048. https://doi.org/10.1016/j.carbon.2009.11.023

[23] https://www.cabotcorp.com

[24] S. Brunauer, P.H. Emmett, E. Teller, Adsorption of gases in multimolecular layers, J. Am. Chem. Soc. 60 (1938) 309–319. https://doi.org/10.1021/ja01269a023

[25] M.M. Dubinin, The equation of the characteristic curve of activated charcoal. Dokl. Akad. Nauk. 55 (1947) 327–329.

[26] J. Landers, G.Y. Gor, A.V. Neimark, Density functional theory methods for characterization of porous materials, Colloids Surf. A Physicochem. Eng. Asp. 437 (2013) 3–32. https://doi.org/10.1016/j.colsurfa.2013.01.007.

[27] K. László, O. Czakkel, K. Josepovits, C. Rochas, E. Geissler, Influence of surface chemistry on the SAXS response of polymer-based activated carbons, Langmuir 21 (2005) 8443–8451. https://doi.org/10.1021/la050389+

[28] D. Massiot, F. Fayon, M. Capron, I. King, S. Le Calvé, B. Alonso, J.-O. Durand, B. Bujoli, Z. Gan, G. Hoatson, Modelling one- and two-dimensional solid-state NMR spectra, Magn. Reson. Chem. 40(1) (2001) 70–76. https://doi.org/10.1002/mrc.984

[29] E.O. Stejskal, J.E. Tanner, Spin Diffusion Measurements: Spin Echoes in the Presence of a Time-Dependent Field Gradient, J. Chem. Phys. 42 (1965) 288–292. https://doi.org/10.1063/1.1695690

[30] M. Thommes, K. Kaneko, A.V. Neimark, J.P. Oliver, F. Rodriguez-Reinoso, J. Rouquerol, K.S.W. Sing, Physisorption of gases, with special reference to the evaluation of surface area and pore size distribution (IUPAC Technical Report). Pure Appl. Chem. 2015, 87, 1051–1069. https://doi.org/10.1515/pac-2014-1117

[31] P.J.F. Harris, I. Suarez-Martinez, Rosalind Franklin, carbon scientist, Carbon 171 (2021) 289–293. https://doi.org/10.1016/j.carbon.2020.09.022

[32] J.D. Bernal, The Structure of Graphite, Proc. Roy. Soc. 106 (1924) 749–773. https://doi.org/10.1098/rspa.1924.0101

[33] A. Oberlin, Carbonization and graphitization, Carbon 22 (1984) 521–541. https://doi.org/10.1016/0008-6223(84)90086-1

[34] C. de Tomas, I. Suarez-Martinez, F. Vallejos-Burgos, M. J. Lopez, K. Kaneko, N. A. Marks, Structural prediction of graphitization and porosity in carbide-derived carbons. Carbon 119, 1 (2017). http://dx.doi.org/10.1016/j.carbon.2017.04.004

[35] C. de Tomas, I. Suarez-Martinez, N.A. Marks, Carbide-derived carbons for dense and tunable 3D graphene networks, App. Phys. Lett. 112 (2018) 251907. https://doi.org/10.1063/1.5030136.

[36] R. Thyagarajan, D.S. Sholl, A database of porous rigid amorphous materials, Chem. Mater. 32 (18) (2020) 8020–8033. https://dx.doi.org/10.1021/acs.chemmater.0c03057

[37] N.J. Corrente, E.L. Hinks, A. Kasera, R. Gough, P.I. Ravikovitch, A.V. Neimark, Modeling adsorption of simple fluids and hydrocarbons on nanoporous carbons, Carbon 197 (2022) 526–533. https://doi.org/10.1016/j.carbon.2022.06.071.

[38] M.A. López-Antón, M. Díaz-Somoano, J.L.G. Fierro, M.R. Martínez-Tarazona, Retention of arsenic and selenium compounds present in coal combustion and gasification flue gases using activated carbons, Fuel Processing Technology 2007, 88, 2007, 799-805

[39] I. Ferrari, A. Motta, R. Zanoni, F.A. Scaramuzzo, F. Amato, E.A. Dalchiele, A.G. Marrani, Understanding the nature of graphene oxide functional groups by modulation of the electrochemical reduction: A combined experimental and theoretical approach, Carbon 203, (2023), 29–38. https://doi.org/10.1016/j.carbon.2022.11.052

[40] R.P. Rocha, O.S.G.P. Soares, J.L. Figueiredo, M.F.R. Pereira, Tuning CNT properties for metal-free environmental catalytic applications, C 2(3) (2016) 17. https://doi.org/10.3390/c2030017

[41] R.P. Rocha, M.F.R. Pereira, J.L. Figueiredo, Characterisation of the surface chemistry of carbon materials by temperature-programmed desorption: An assessment, Catal. Today 418 (2023) 114–136. https://doi.org/10.1016/j.cattod.2023.114136

[42] P. Solís-Fernández, J. I. Paredes, S. Villar-Rodil, L. Guardia, M. J. Fernández-Merino, G. Dobrik, L. P. Biró, A. Martínez-Alonso, J. M. D. Tascón, Global and local oxidation behavior of reduced graphene oxide, J. Phys. Chem. C 2011, 115, 16, 7956–7966

[43] Y. Xu, T. Watermann, H-H. Limbach, T. Gutmann, D. Sebastiani, G. Buntkowsky, Water and small organic molecules as probes for geometric confinement in well-ordered mesoporous carbon materials Phys. Chem. Chem. Phys. 16 (2014) 9327–9336. https://doi.org/10.1039/C4CP00808A

[44] K. Rottger, A. Endriss, J. Ihringer, S. Doyle, W.F. Kuhs, Lattice Constants and Thermal Expansion of H_2O and D_2O Ice I*h* Between 10 and 265 K, Acta Crystallogr. B 68 (2012) 644–648. https://doi.org/10.1107/S0108768111046908

[45] O. Kratky, O. Glatter, Small angle X-ray scattering, Academic Press (1982) 17–51.

[46] V. Luzzati, J. Witz, A. J. Nicolaieff, Détermination de la masse et des dimensions des protéines en solution par la diffusion centrale des rayons X mesurée à l'échelle absolue:

Exemple du lysozyme, Mol. Biol. 3 (1965) 367–378.

[47] D.D. Do, H.D. Do, A model for water adsorption in activated carbon, Carbon 38 (2000) 767–770. https://doi.org/10.1016/S0008-6223(99)00159-1

[48] T. Iiyama, K. Nishikawa, T. Otowa, K. Kaneko, An Ordered Water Molecular Assembly Structure in a Slit-Shaped Carbon Nanospace, J. Phys. Chem. 99 (1995) 10075–10076. https://doi.org/10.1021/j100025a004

[49] K. Kaneko, Y. Hanzawa, T. Iiyama, T. Kanda, T. Suzuki, Cluster-Mediated Water Adsorption on Carbon Nanopores, Adsorption 5 (1999) 7–13. https://doi.org/10.1023/A:1026471819039

[50] T. Ohba, H. Kanoh, K. Kaneko, Cluster-Growth-Induced Water Adsorption in Hydrophobic Carbon Nanopores, J. Phys. Chem. B 108 (2004) 14964–14969. https://doi.org/10.1021/jp048323v

SUPPLEMENTARY MATERIAL

Table S1 Numerical data deduced from Figure 6

R1 43.2%

^{1}H signal	Chemical shift (ppm)	Width (ppm)	Rel. Int. (%)	Abs. Int. (2.64)
1	-3.50	2.71	56	1.49
2	-3.99	1.29	29	0.78
3	-5.23	11.07	14	0.37
4 (bulk water)	-	-	-	-

R1 84.3 %

^{1}H signal	Chemical shift (ppm)	Width (ppm)	Rel. Int. (%)	Abs. Int. (12.76)
1	-3.52	2.18	45	5.69
2	-3.62	1.42	44	5.63
3	-4.24	5.50	11	1.44
4 (bulk water)	4.79	0.05	0	0.01

OX 43.2 %

^{1}H signal	Chemical shift (ppm)	Width (ppm)	Rel. Int. (%)	Abs. Int. (3.68)

1	-2.28	2.09	74	2.73
2	-2.74	1.03	8	0.31
3	-3.38	6.47	17	0.64
4 (bulk water)	-	-	-	-

OX 84.3 %

^{1}H signal	Chemical shift (ppm)	Width (ppm)	Rel. Int. (%)	Abs. Int. (9.06)
1	-2.43	1.75	75	6.79
2	-2.74	0.97	9	0.80
3	-2.85	4.55	16	1.46
4 (bulk water)	4.79	0.06	0	0.01

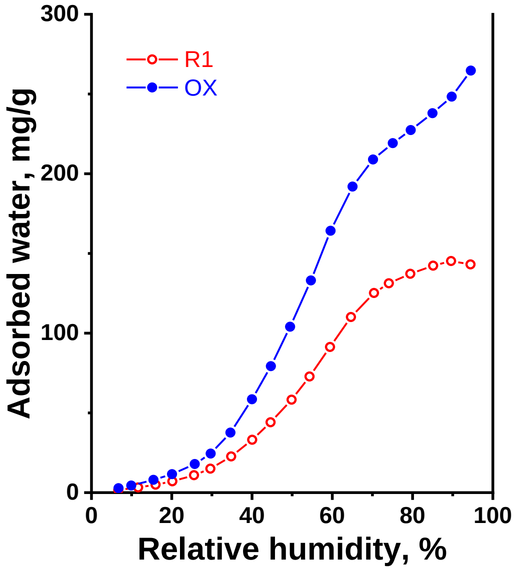

Figure S1 Water vapour isotherms measured at 20 ºC on the granules, after degassing for 24 hours at 2.7 Pa at room temperature on a volumetric Hydrosorb apparatus (Quantachrome) with vapour generated at 100 ºC.

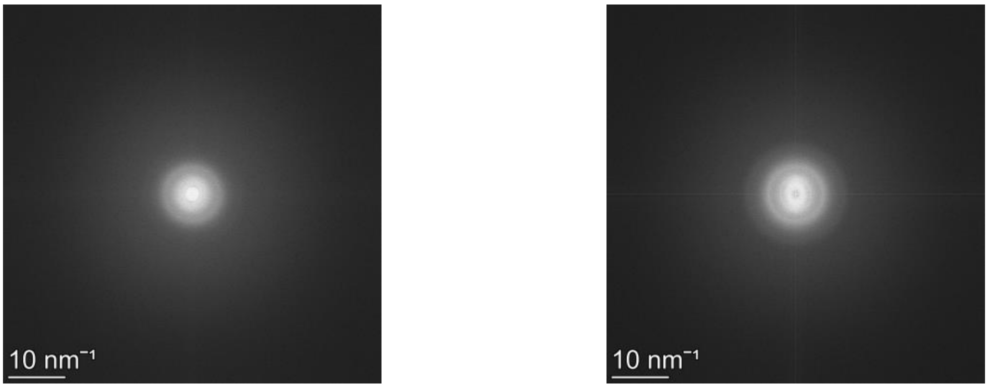

a **b**

Figure S2. FFT images of the a) R1 and b) OX samples corresponding to Figures F2a and F2b, respectively.

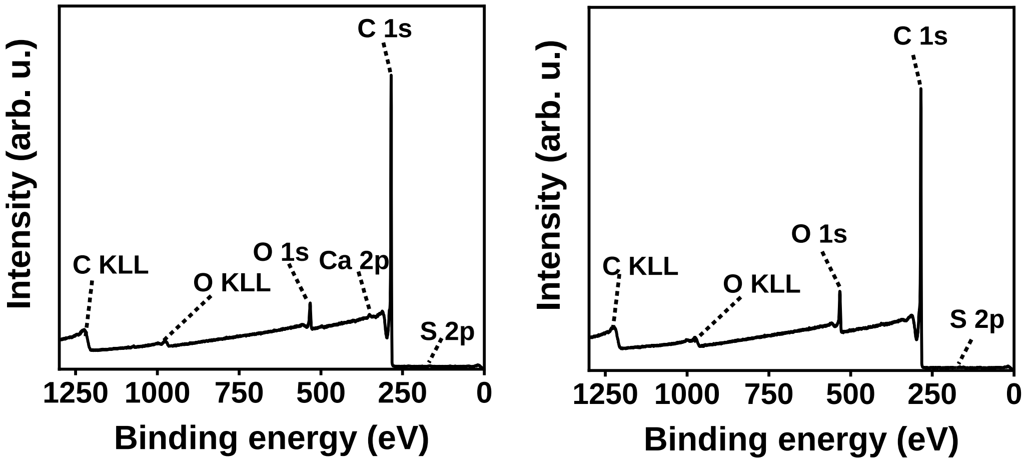

a **b**

Figure S3. XPS survey spectra of **(a)** untreated and **(b)** oxidized Norit. The main XPS and Auger bands have been labeled for clarity.

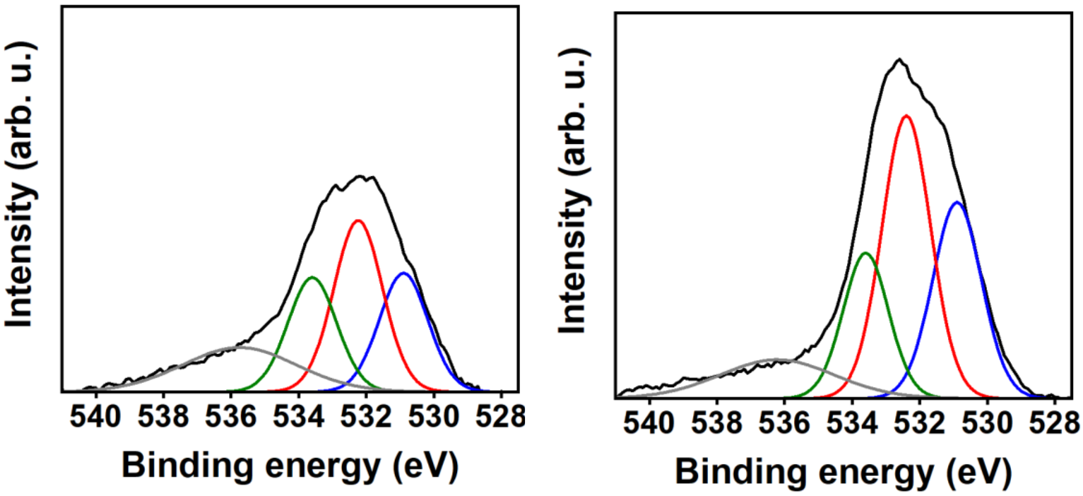

Figure S4. Deconvolution of high-resolution O 1s core level XPS spectra for **(a)** R1 and **(b)** OX into four components: doubly bonded oxygen OI (blue), singly bonded oxygen in alcohols, ethers and peroxides (OII red); singly bonded oxygen in acids, esters and hydroperoxides (OIII green), and peroxyacid, peroxyester, and/or charge effect (O* gray).

OI, OII, OIII and O* are assigned, respectively, in order of increasing binding energy to doubly bonded oxygen (~531 eV); singly bonded oxygen in alcohols, ethers and peroxides (~+1 eV); singly bonded oxygen in acids, esters and hydroperoxides (~+2-2.5 eV), and peroxyacid, peroxyester, and/or charge effect (~+4 eV) [46]. The percentages of OI, OII, OIII and O* are as follows: 23, 34, 22 and 21% for R1 and 28, 40, 19 and 13% for OX. Considering that there is 30% more oxygen in OX than in R1, the amount of all oxygen containing functionalities except for O* increases with the oxidation.

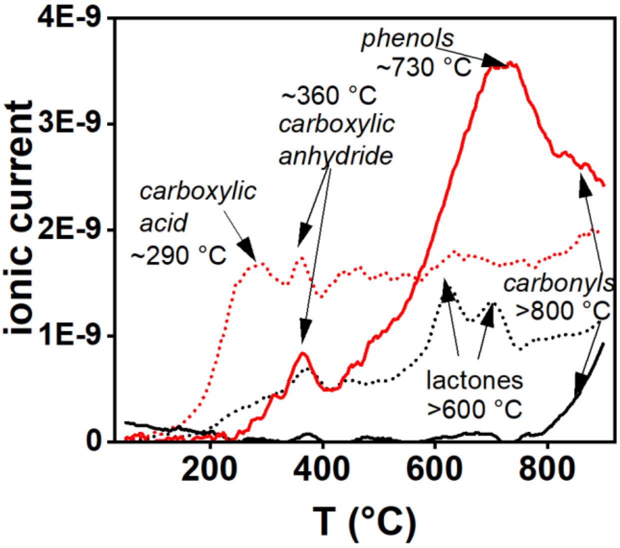

Figure S5. CO (M/Z=28, solid line) and CO_2 (M/Z=44, dotted line) release of the carbon samples from TG/MS analysis for R1 (black) and OX (red) materials.

The presence of *carboxylic acids* in both R1 and OX is confirmed by the CO_2 release below 400 °C. The enhanced evolution observed for OX indicates a higher content in such functional groups. While isolated carboxyls are directly released upon heating, those having another carboxylic group nearby could undergo dehydration first to yield a more thermally stable carboxylic anhydride. However, as heating proceeds, carboxylic anhydrides will also decompose between 350 and 600 °C by releasing one CO and one CO_2 molecules. Thus, *carboxylic anhydrides* are revealed by the simultaneous appearance of similar bands in both CO and CO_2 profiles. In this work, they are clearly detected for OX and barely detectable in the case of R1. This is not unexpected from the fact that the oxygen functionalities on charcoal are expected to have a certain thermal stability as the material itself was prepared through a heat treatment. On the contrary, OX was obtained at room temperature and did not undergo further thermal treatment. Thus, it is expected that it contains a higher amount of less thermally stable oxygen functionalities.

In the case of R1, the most pronounced bands are CO_2 release bands above 600 °C, usually related to the presence of *lactones*. These could come from the condensation of neighboring carboxyl and phenol groups

Phenol groups may be observed by the release of CO in a middle temperature range (500–750 °C), while *carbonyl/quinone* groups release CO above 700 °C. As the experiments were performed at a rather high heating rate (20 °C/min) compared to the usual 5–10 °C/min used for TPD experiments, the temperature ranges at which the different functional groups are detected could appear at higher temperatures than those found for experiments performed at lower temperatures. Thus, the wide band at ~730 °C in the CO profile of OX is attributable to phenols, while the release of CO above 800 °C for both materials could be related to carbonyl/quinone.

Pyrone-type groups could be present, but may go unnoticed as they release CO at temperatures above 950 °C. This range is not covered in the TG/MS observations.